Comparative study for reaction dynamics of ^{6}He projectiles scattered from ^{58}Ni, ^{64}Zn, and ^{120}Sn targets

D. Elbehari, S. S. Saad and Sh. Hamada*

Faculty of Science, Tanta University, Tanta, Egypt.
**e-mail: sh.m.hamada@science.tanta.edu.eg*

Received 25 January 2026; accepted 26 March 2026

We perform a comparative analysis of the elastic scattering of ^{6}He projectiles from ^{58}Ni, ^{64}Zn, and ^{120}Sn targets at energies (9-21.7 MeV, 9.84-17.9 MeV, and 17.4-20.5 MeV, respectively). The exotic two-neutron halo structure of ^{6}He strongly influences the scattering dynamics in this energy regime. Using a range of microscopic and cluster-based potentials–including the double-folding potential (DFP), São Paulo potential (SPP2), Brazilian nuclear potential (BNP), and a cluster folding potential (CFP)–we analyze the angular distributions to explore the effects of ^{6}He breakup and the resulting dynamic polarization. Our study systematically examines the emergence of breakup threshold anomalies, the behavior of the optical potential parameters, and the role of target mass and charge in modifying the effective interaction. The CFP, which explicitly incorporates the α + 2n cluster configuration, systematically yields larger reaction cross-sections across all systems and energies, though the magnitude of this effect is modest and often comparable to statistical uncertainties. This systematic trend nevertheless underscores the importance of cluster degrees of freedom in describing halo-nucleus collisions.

Keywords: ^{6}He breakup; normal and breakup threshold anomalies; double and cluster folding potentials.

DOI: https://doi.org/10.31349/RevMexFis.72.041201

1. Introduction

The advent of radioactive ion beam (RIB) facilities has opened a new frontier in nuclear physics, enabling the study of exotic nuclei far from stability. Among these, a fascinating class known as halo nuclei–characterized by a diffuse cloud of one or two weakly bound nucleons surrounding a tightly bound core–offers a unique laboratory to investigate novel structural features and reaction mechanisms not observed in stable isotopes. Among these, the ^{6}He isotope stands as a paradigmatic example of a two-neutron halo nucleus. With a low two-neutron separation energy of only 0.973 MeV and a matter radius of approximately 2.33 fm–significantly larger than its α-particle core–^{6}He exhibits a pronounced Borromean structure, where the three constituents (α + n + n) are bound despite the absence of any bound two-body subsystem. This delicate, spatially extended structure makes ^{6}He exceptionally sensitive to the external field of a target nucleus during collisions, leading to distinctive and enhanced reaction processes.

Investigating the scattering of ^{6}He from a range of target nuclei is a powerful diagnostic tool that reveals the intimate connection between nuclear structure and reaction mechanisms. By systematically studying collisions with targets spanning different masses and charge distributions–such as ^{58}Ni, ^{64}Zn, and ^{120}Sn–we can disentangle the varying influences of Coulomb and nuclear forces on the fate of this fragile projectile. Each target offers a different lens through which to observe how the halo's diffuse tail interacts with the mean field of the target, how the probability of breakup evolves with the strength of the Coulomb field, and which reaction channels–be it elastic scattering, direct breakup, or neutron transfer–dominate under different conditions.

At the heart of this inquiry lies a fundamental quest to understand how the exotic structure of ^{6}He reshapes the effective interaction between the two colliding nuclei. Its weak binding leads to a strong coupling to the breakup continuum, which in turn dynamically polarizes the nucleus-nucleus potential, introducing long-range absorption and effectively modifying the nucleus-nucleus interaction. This necessitates moving beyond conventional optical models and embracing advanced, few-body reaction frameworks like the Continuum Discretized Coupled Channels method to faithfully interpret experimental observations.

Furthermore, the significant yield of α-particles observed in reactions with heavier targets like ^{120}Sn prompts critical questions about the dominant production mechanisms, compelling us to distinguish between direct projectile dissociation and neutron-stripping processes that leave an α-particle in the final state. By comparing results across systems like ^{6}He + ^{58}Ni, ^{64}Zn, and ^{120}Sn, we can map out systematic trends, test the robustness of our theoretical models across a spectrum of masses, and build a coherent picture of halo-induced reaction dynamics.

This work investigates the scattering mechanisms of ^{6}He from ^{58}Ni, ^{64}Zn, and ^{120}Sn, targets across various energies, analyzing angular distributions (ADs) for the ^{6}He + ^{58}Ni system at laboratory energies ($E_{\rm lab}$) of 9 [1], 10 [2], 12.2, 16.5, and 21.7 MeV [3], the ^{6}He + ^{64}Zn system at $E_{\rm lab}$ of 9.84 and 13.56 MeV [4], 14.85 and 17.9 MeV [5], and the ^{6}He + ^{120}Sn system at $E_{\rm lab}$ = 17.4, 18.05, 19.8 and 20.5 [6] using multiple potential approaches.

Additionally, these systems were studied theoretically [7–10]. Su *et al.* [7] developed a global phenomenological optical model potential (OMP) for ^{6}He based on Woods-Saxon (WS) forms for the real part and derivative WS forms for the imaginary part. The parameters were optimized by fitting available experimental data, including reaction cross-sections and elastic scattering ADs, for target nuclei in the mass range $6 \leq A \leq 209$ and incident energies up to 250 MeV. The OMP parameters are energy-dependent and include geometry parameters constrained by physical considerations. Guo *et al.* [8] developed a microscopic optical potential (MOP) for ^{6}He using a parameter-free folding model. The potential is constructed by folding an isospin-dependent nucleon MOP, based on Skyrme interactions, with a harmonic oscillator description of ^{6}He's internal structure. The ^{6}He MOP is applied to calculate elastic scattering and reaction cross sections for targets from ^{12}C to ^{209}Bi at energies up to 350 MeV. While the MOP yields reasonable results, it generally underperforms compared to a phenomenological global optical potential (GOP) fitted to data. Sensitivity analysis reveals that scattering is most sensitive to the nuclear surface region. Lichtenthaler *et al.* [9] analyzed elastic scattering ADs of the neutron-halo nucleus ^{6}He on light (^{9}Be), medium (^{58}Ni), and heavy (^{120}Sn) targets using a simplified diffractive model for the S-matrix. The model parameterizes the S-matrix in angular momentum space with three parameters: the grazing angular momentum (Λ), diffuseness (Δ), and a nuclear phase (α). This approach offers a computationally efficient alternative to other methods such as Continuum Discretized Coupled Channels (CDCC) calculations. Descouvemont [10] presented a microscopic continuum discretized coupled-channel (MCDCC) study of low-energy ^{6}He elastic scattering on ^{27}Al, ^{58}Ni, ^{120}Sn, and ^{208}Pb. The ^{6}He projectile is described as an antisymmetrized α+n+n cluster system using the resonating group method, with its continuum discretized into pseudostates. The model uses only standard nucleon-target optical potentials, requiring no adjustable parameters. The calculations reproduce experimental cross sections well and reveal a strong target-mass dependence of breakup effects: they are minimal for light targets (^{27}Al) but crucial for heavy ones (^{208}Pb). This trend is analyzed through scattering matrices and explained using a simple sharp-cutoff model. Equivalent polarization potentials, extracted from the calculations, show a repulsive real part and a long-range absorptive imaginary component, both increasing with target mass.

In this work, we investigate the elastic scattering of ^{6}He from ^{58}Ni, ^{64}Zn, and ^{120}Sn targets at energies in the vicinity of the Coulomb barrier. We analyze available angular distribution data using a hierarchy of interaction potentials: the double-folding potential (DFP), the São Paulo potential (SPP2), the Brazilian nuclear potential (BNP), and a cluster folding potential (CFP) that explicitly incorporates the α+2n structure of ^{6}He. Our aim is to explore the manifestation of breakup effects – particularly the breakup threshold anomaly (BTA) – and to evaluate the importance of cluster degrees of freedom in describing the scattering of this archetypal halo nucleus. This systematic study not only illuminates the reaction dynamics of ^{6}He but also provides a valuable benchmark for understanding more complex neutron-rich exotic nuclei. The manuscript is organized as follows: Section 2 outlines the theoretical framework and the optical potentials employed. Section 3 presents and discusses the results for each target system. Finally, Sec. 4 summarizes the principal conclusions of this comparative study.

2. Theoretical framework and implemented potentials

The elastic scattering ADs for the ^{6}He + ^{58}Ni ($E_{\rm lab}$ = 9-21.7 MeV) [1–3], ^{6}He + ^{64}Zn ($E_{\rm lab}$ = 9.84-17.9 MeV) [4, 5], and ^{6}He + ^{120}Sn ($E_{\rm lab}$ = 17.4-20.5 MeV) [6] systems have been reanalyzed through a systematic progression of theoretical approaches. We employ a hierarchy of potentials, ranging from sophisticated microscopic methods – such as the energy-independent Brazilian Nuclear Potential (BNP), the energy-dependent São Paulo Potential (SPP2), and the conventional Michigan three-term Yukawa double-folding potential (DFP) – to the cluster folding potential (CFP), which is based explicitly on the α + 2n cluster structure of the ^{6}He projectile. This methodological sequence offers complementary insights into the scattering dynamics and helps identify the interaction potentials that best reproduce the experimental ADs. All calculations were performed with the FRESCO code [11], supplemented by the SFRESCO interface for χ^2 minimization, which allowed for accurate extraction of the optimal potential parameters.

2.1. Microscopic DFP, SPP2, and BNP

In the first stage of the analysis, the elastic scattering ADs for ^{6}He + T, (T = ^{58}Ni, ^{64}Zn, ^{120}Sn) were examined within several microscopic optical potentials. The central interaction consists of a Coulomb term ($V_C(r)$) and a nuclear term ($V_N(r)$). The nuclear part contains a real component that governs the scattering and an imaginary component that accounts for absorption. By using microscopic constructions, we avoid the ambiguities – both continuous and discrete – that often appear in conventional WS parameterizations. The double folding potential (DFP) is built by folding the projectile and target ground-state densities with an effective nucleon-nucleon (v_{NN}) interaction:

$$V^{DF}(R) = \int\int \rho_P(\vec{r}_P)\rho_T(\vec{r}_T)\nu_{NN} \times (\vec{R} - \vec{r}_P + \vec{r}_T)d\vec{r}_P d\vec{r}_T, \quad (1)$$

where $\vec{R}$ is the separation vector between the centers of mass of the projectile and target, $\vec{r}_P$ and $\vec{r}_T$ are internal coordinates of the projectile and target nucleons, respectively. The functions ρ_P and ρ_T are the ground-state point-nucleon densities of projectile and target, respectively. For the NN in-

teraction, we adopt the CDM3Y2 form [12], which is based on the M3Y-Paris potential and includes direct and exchange contributions:

$$v_D(s) = 11061.625\frac{e^{-4s}}{4s} - 2537.5\frac{e^{-2.5s}}{2.5s},$$
$$v_{EX}(s) = -1524.25\frac{e^{-4s}}{4s} - 518.75\frac{e^{-2.5s}}{2.5s} - 7.8474\frac{e^{-0.7072s}}{0.7072s}, \quad (2)$$

Here, v_D represents the direct part of the interaction, which is independent of energy and corresponds to the exchange of a single meson between nucleons. The term v_{EX} is the exchange part, which arises from the antisymmetrization of the nucleon-nucleon wave function and accounts for the knock-out exchange of the interacting nucleons; it carries an explicit energy dependence due to the momentum-dependence of the exchange process. The CDM3Y2 interaction incorporates a density-dependent factor $F(\rho)$ that accounts for medium effects [12]:

$$F(\rho) = 0.3346[1 + 3.0357e^{-3.0685\rho} - \rho], \quad (3)$$
$$V^{DF}_{D(EX)}(\rho, s) = F(\rho)V^{DF}_{D(EX)}(s), \quad (4)$$

where ρ is the nuclear-matter density, and s is the separation between two interacting nucleons. We have also employed the São Paulo Potential version 2 (SPP2) [13–16], which similarly folds the projectile and target densities with an interaction potential ν^{SPP2}_{NN} [13]:

$$\nu^{SPP2}_{NN}(\vec{r}) = -U_0 e^{-(r/a)^2} e^{-4V^2/C^2}, \quad (5)$$

with strength parameter U_0= 735.813 MeV and the range parameter a = 0.5 fm in its updated SPP2 version [13]. Here, V is the local relative velocity between the colliding nuclei, and C is the speed of light. The density distributions of the ^{6}He projectile $\rho_P(r_P)$ and target $\rho_T(r_T)$ nuclei (^{58}Ni, ^{64}Zn, ^{120}Sn) were obtained from the Dirac-Hartree-Bogoliubov (DHB) model [17] using the REGINA code. In addition, the ADs data for the considered nuclear systems are reanalyzed using the Brazilian Nuclear Potential (BNP), which in its simplest Gaussian representation reads

$$\nu^{BNP}_{NN}(R) = -U_0 e^{-(R/a)^2}, \quad (6)$$

with U_0=87.226 MeV and a=0.95 fm.

2.2. Cluster folding potential (CFP)

The exotic ^{6}He nucleus displays a pronounced cluster structure – an α-core surrounded by two valence neutrons – with a two-neutron separation energy of only ≈0.975 MeV. To explore the consequences of this cluster configuration on the scattering dynamics, we have implemented a cluster folding model (CFM). Within this model, the real and imaginary parts of the cluster folding potential (CFP) are generated by folding appropriate α+T and 2n+T optical potentials, chosen to describe the experimental data for the corresponding subsystems at energies equal to two-thirds and one-third of the incident ^{6}He energy, respectively. Explicitly, the CFP is constructed as:

$$V^{CF}(\mathbf{R}) = \int \left[V_{\alpha-T}\left(\mathbf{R} - \frac{1}{3}\mathbf{r}\right) + V_{2n-T}\left(\mathbf{R} + \frac{2}{3}\mathbf{r}\right)\right] \times |\chi_{\alpha-2n}(\mathbf{r})|^2 d\mathbf{r},$$
$$W^{CF}(\mathbf{R}) = \int \left[W_{\alpha-T}\left(\mathbf{R} - \frac{1}{3}\mathbf{r}\right) + W_{2n-T}\left(\mathbf{R} + \frac{2}{3}\mathbf{r}\right)\right] \times |\chi_{\alpha-2n}(\mathbf{r})|^2 d\mathbf{r}, \quad (7)$$

The $\chi_{\alpha-2n}(\mathbf{r})$ is the internal wave function of ^{6}He in its α+2n configuration. This wave function, representing a $2S$ state, was generated by the standard "well-depth" procedure using a real Woods-Saxon potential with radius $R = 1.83$ fm and diffuseness $a = 0.65$ fm [18]. The required α+T and 2n+T potentials were taken from the energy-independent BNP [13] with the standard normalizations 1.0 (real part) and 0.78 (imaginary part) [19]. The density distributions for the deuteron (as a surrogate for the 2n pair), α-particle, ^{6}He, and the three targets, calculated with the DHB model [17], are displayed in Fig. 1.

Figure 1 shows the point-nucleon density distributions, ρ(r), for the deuteron (^{2}H), α-particle (^{4}He), ^{6}He, and the three targets ^{58}Ni, ^{64}Zn, and ^{120}Sn, as computed within the DHB framework [17]. The extended tail of the ^{6}He density is clearly visible, reflecting its two-neutron halo structure. In contrast, the α-particle and the stable targets exhibit a sharp fall-off characteristic of tightly bound systems. These densities serve as the essential inputs for the folding calculations, linking the intrinsic structure of the colliding nuclei directly to the nucleus-nucleus interaction potential.

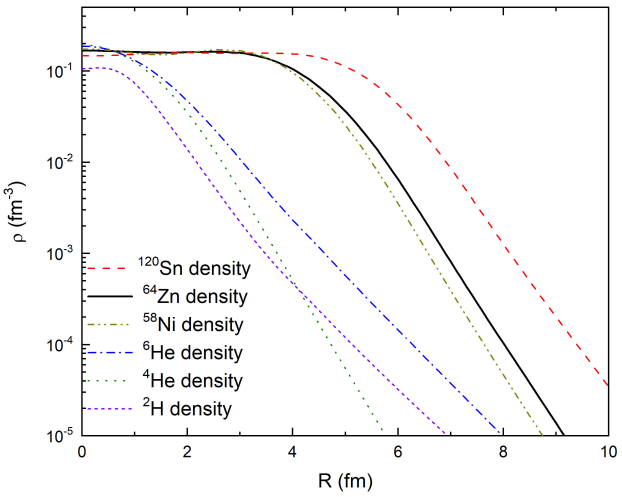

FIGURE 1. Density distributions for ^{2}H, ^{4}He, ^{6}He, ^{58}Ni, ^{64}Zn, and ^{120}Sn nuclei calculated using the DHB model.

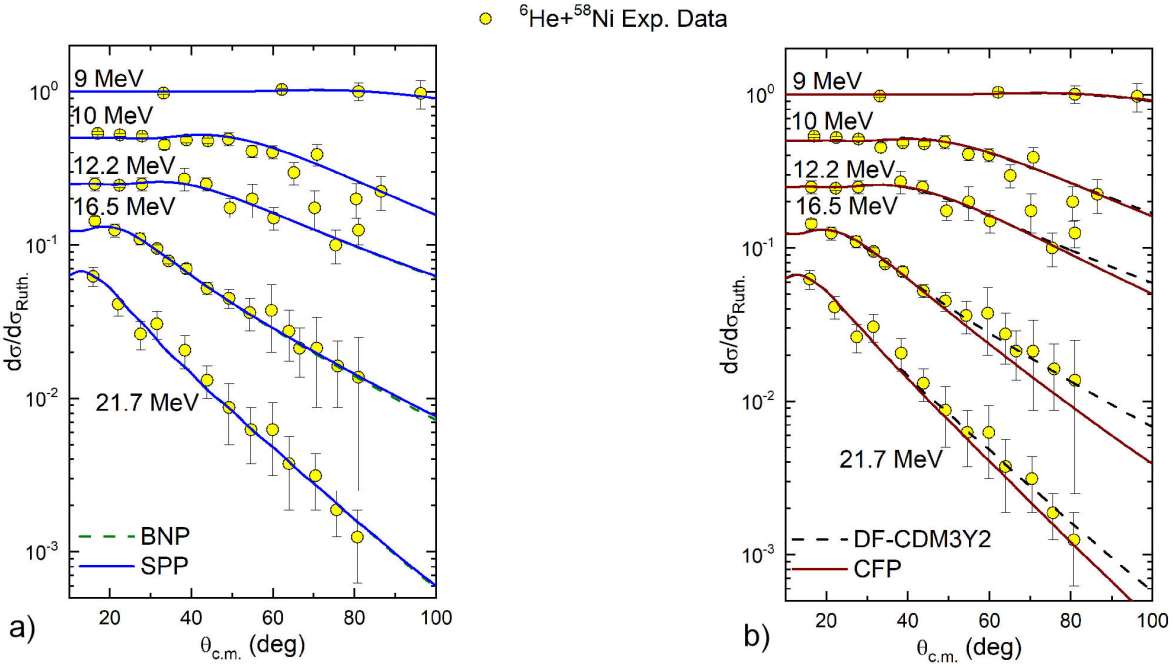

FIGURE 2. Comparison between ^{6}He + ^{58}Ni elastic scattering ADs (circles) and calculations within both BNP and SPP2 presented in panel a), while the results within DF-CDM3Y2 and CFP are presented in panel b).

3. Results and discussion

The elastic scattering ADs for ^{6}He + ^{58}Ni system at $E_{\rm lab}$ between 9 and 21.7 MeV [1–3], the ^{6}He + ^{64}Zn system at $E_{\rm lab}$ between 9.84 and 17.9 MeV [4, 5], and ^{6}He + ^{120}Sn system at $E_{\rm lab}$ between 17.4 and 20.5 MeV [6] are analyzed within the framework of DFP of different NN interaction potentials, namely, BNP, SPP2, and CDM3Y2 as well as CFP. The employed central potential consists of a Coulomb repulsive potential and an attractive nuclear potential. It is well-documented that preparing the interaction potential using microscopic methods such as DFP and CFP is always recommendable for avoiding the different parameter ambiguities (continuous and discrete) that arise from the usual six parameters of WS calculations. The real parts of the DF-CDM3Y2, SPP2, and BNP were computed using Eq. (1) with the interaction potentials presented in Eqs. (2), (5), and (6), respectively, and the imaginary parts were taken as a factor times the real parts. While, for the CFP, the real and imaginary CFP arts were computed using Eq. (7) . The real and imaginary parts of DFPs and CFP are identified in terms of the normalization factors, N_R and N_I, respectively. As a first step, the available ^{6}He + T ADs [1–6] were described within folding potentials whose real and imaginary parts strengths were allowed to freely change in the range 0.1 to 2.0 until the best agreement between data and results is obtained. The FRESCO code [11] was upgraded with χ^2 minimization SFRESCO. The quality of fitting and hence the optimal potential parameters were obtained by minimizing the χ^2 value which defines the deviation between experimental data and calculations, and defined as follow:

$$\chi^2 = \frac{1}{N}\sum_{i=1}^{N}\left[\frac{\sigma(\theta_i)^{\rm cal} - \sigma(\theta_i)^{\rm exp}}{\Delta\sigma(\theta_i)}\right]^2, \qquad (8)$$

where $\sigma(\theta_i)^{\rm exp}$ and $\sigma(\theta_i)^{\rm cal}$ are the experimental and calculated cross sections,$\Delta\sigma(\theta_i)$ is the relative uncertainty in experimental data.

The main advantage of such methodology is that it could give a rather clear energy dependence on the imaginary potential strength and consequently a better conclusion about the presence/absence of the BTA in ^{6}He + T systems can be drawn. The following form describes the shape of the central potential:

$$U(R) = V_C(R) - N_R V^{DF}(R) - iN_I V^{DF}(R), \qquad (9)$$

The comparisons between the experimental ADs data for the ^{6}He + T systems and the theoretical results within the aforementioned folded-potentials of two adjustable parameters, N_R and N_I are illustrated in Figs. 2, 4, and 6. The optimal values for N_R and N_I normalization factors are listed in Tables I, II, and III, for the three considered systems: ^{6}He + ^{58}Ni, ^{6}He + ^{64}Zn, and ^{6}He + ^{120}Sn, respectively. The reaction cross section (σ_R) values are also given in the tables.

3.1. ^{6}He+^{58}Ni system

The elastic scattering of ^{6}He from the medium-mass ^{58}Ni target presents a contrasting scenario to the heavy ^{120}Sn system, offering insights into the role of the Coulomb interaction in halo nucleus dynamics. As detailed in Table I and Fig. 2, the optimal normalization parameters (N_R and N_I) for the BNP, SPP2, DFP-CDM3Y2, and CFP potentials exhibit a clear and

TABLE I. Optimal potential parameters for ^{6}He + ^{58}Ni system within BNP, SPP2, DFP-CDM3Y2, and CFP. The σ_R values are displayed with their estimated uncertainties.

E (MeV)		N_R	N_I	χ^2/N	σ_R (mb)
9	BNP	0.374 ± 0.081	0.134 ± 0.122	0.55	126 ± 60
	SPP2	0.377 ± 0.162	0.127 ± 1.336	0.54	125 ± 301
	DFP	0.257 ± 0.077	0.100 ± 1.854	0.55	127 ± 430
	CFP	0.221 ± 0.046	0.118 ± 0.092	0.57	116 ± 64
10	BNP	1.507 ± 0.632	2.000 ± 0.166	2.70	859 ± 70
	SPP2	1.573 ± 0.632	2.000 ± 0.168	2.72	856 ± 70
	DFP	0.829 ± 0.580	2.000 ± 0.203	2.41	898 ± 82
	CFP	0.388 ± 0.293	2.000 ± 0.158	2.31	918 ± 81
12.2	BNP	0.100 ± 0.310	1.003 ± 0.367	0.48	961 ± 148
	SPP2	0.100 ± 0.334	1.024 ± 0.381	0.48	960 ± 151
	DFP	0.100 ± 0.177	0.678 ± 0.258	0.50	957 ± 138
	CFP	0.100 ± 0.072	0.791 ± 0.251	0.59	970 ± 127
16.5	BNP	0.100 ± 0.394	1.957 ± 1.340	0.26	1735 ± 240
	SPP2	0.100 ± 1.336	2.000 ± 1.808	0.25	1730 ± 346
	DFP	0.100 ± 0.180	1.342 ± 0.222	0.26	1724 ± 85
	CFP	0.100 ± 0.031	1.500 ± 0.196	0.48	1749 ± 65
21.7	BNP	0.396 ± 0.168	1.771 ± 1.603	0.32	2087 ± 274
	SPP2	0.447 ± 0.190	1.771 ± 1.634	0.33	2077 ± 273
	DFP	0.274 ± 0.125	1.257 ± 0.626	0.32	2082 ± 173
	CFP	0.100 ± 0.026	1.662 ± 0.571	0.42	2136 ± 158

systematic energy dependence across the investigated range ($9 - 21.7$ MeV).

At the lowest energy of 9 MeV, which lies just above the Coulomb barrier (8.35 MeV), all potentials require a strong suppression of the real potential strength ($N_R \sim 0.22 - 0.38$) to reproduce the data. Concurrently, the imaginary normalization N_I is found to be very small ($N_I \sim 0.10 - 0.13$), indicating minimal absorption at this energy. This pattern is consistent with the expectations for a tightly bound system at energies well below the barrier, where the imaginary potential is typically weak. The fact that the weakly-bound ^{6}He projectile exhibits this behavior suggests that at this very low energy, the breakup channel is not significantly open, and the interaction is dominated by the far-tail of the nuclear potential where the halo extension plays a minor role.

As the energy increases from 9 MeV to 10 MeV and further to 12.2, 16.5, and 21.7 MeV, a marked evolution is observed. The required strength of the imaginary part increases dramatically. For instance, within the DFP-CDM3Y2 model, N_I rises from 0.10 at 9 MeV to ~ 2.00 at 10 MeV, before settling to values of 0.68, 1.34, and 1.26 at the higher energies. This rapid rise in absorption near the barrier is a fingerprint of the BTA, where coupling to the near-threshold breakup continuum leads to a significant enhancement of the imaginary potential. The real part normalization N_R, after the initial strong reduction at 9 MeV, also shows an intriguing non-monotonic behavior. It becomes larger at 10 MeV ($N_R \sim 0.83$ for DFP) before being driven to its lower bound of 0.10 at 12.2 and 16.5 MeV, and then increasing slightly again at 21.7 MeV. This complex behavior, particularly the persistent need for a reduced real strength ($N_R < 1$) at most energies, points to the repulsive dynamical polarization potential (DPP) generated by the strong coupling to the breakup channel. The DPP effectively "renormalizes" the bare folding potential, making the real interaction less attractive.

Comparing the performance of the different potentials, the χ^2/N values in Table I indicate that all four models (BNP, SPP2, DFP, CFP) provide a quantitatively good description of the angular distributions at most energies, with χ^2 typically below 1 for energies above 10 MeV. However, the CFP, which explicitly incorporates the α+2n cluster structure of ^{6}He, consistently yields reaction cross-sections (σ_R) that are marginally higher than those from the structureless density-folding models (BNP, SPP2, DFP), especially at the highest energies. This suggests that the cluster treatment captures additional reaction flux, likely into channels like neutron transfer or specific breakup configurations, which are effectively lumped into a stronger absorption in the optical model picture. The systematic success of the CFP underscores the importance of the cluster degree of freedom in describing the scattering of this Borromean halo nucleus, even for a medium-mass target like ^{58}Ni.

To further elucidate the energy dependence of the optical potential parameters and the manifestation of the BTA, Fig. 3 presents the real and imaginary normalization factors N_R and N_I extracted from the optical model calculations for the ^{6}He

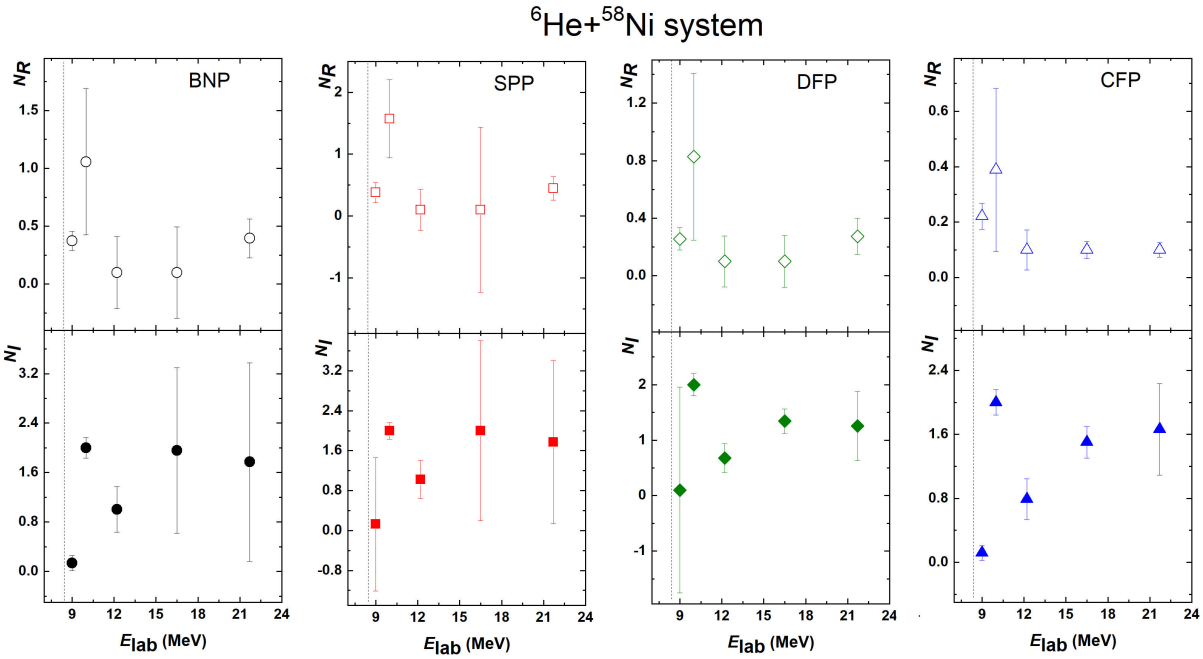

FIGURE 3. Real (upper panel) and imaginary (lower panel) normalization factors N_R and N_I extracted from the optical model calculations for the ^{6}He + ^{58}Ni system as functions of the laboratory energy. Results are shown for the BNP (circles), SPP2 (squares), DFP-CDM3Y2 (diamonds), and CFP (triangles) potentials.

+ ^{58}Ni system as functions of the laboratory energy. The vertical dashed line at $E_{\rm lab} \sim 8.35$ MeV indicates the laboratory energy corresponding to the Coulomb barrier in the center-of-mass frame ($V_B = 7.57$ MeV) obtained for the respective system with the SPP2.

The upper panel of Fig. 3 shows the real normalization factor (N_R). For all four potentials, N_R is systematically less than unity across most of the energy range, reflecting the presence of a repulsive dynamical polarization potential (DPP) generated by the coupling of the elastic channel to the breakup continuum. At the lowest energy (9 MeV), which is slightly above the barrier (8.35 MeV), N_R values are strongly suppressed $0.2 - 0.4$. As the energy increases to 10 MeV, N_R rises for most potentials, reaching values near or above unity for BNP and SPP2, before decreasing again at higher energies. This non-monotonic behavior reflects the complex interplay between nuclear and Coulomb contributions to the DPP as the energy varies through the barrier region.

The lower panel of Fig. 3 displays the imaginary normalization factor N_I. At 9 MeV, just above the barrier, N_I is small $0.1-0.13$ for all potentials, indicating minimal absorption. As the energy increases to 10 MeV, N_I rises dramatically to values near 2.0, reflecting the opening of breakup channels. This rapid increase in absorption near the barrier is characteristic of the BTA. At higher energies (12.2 to 21.7 MeV), N_I remains elevated but shows some variation, with values generally between 0.7 and 2.0 depending on the potential and energy. Overall, the energy dependence of N_I for the ^{6}He + ^{58}Ni system provides evidence of the BTA, with a sharp rise in absorption as the energy increases above the barrier, followed by sustained absorption at higher energies. The behavior of N_R, with values generally below unity, confirms the presence of a repulsive DPP that renormalizes the bare folding potential.

3.2. ^{6}He+^{64}Zn system

The scattering of ^{6}He from the ^{64}Zn target provides a critical intermediate case between the medium-mass ^{58}Ni and the heavy ^{120}Sn systems. With a charge (Z=30) and mass slightly higher than ^{58}Ni (Z=28), it allows us to isolate trends related to the increasing Coulomb force while keeping the nuclear size scale relatively similar. The extracted potential parameters in Table II and the corresponding fits in Fig. 4 reveal distinct features for this system across the measured energy range (9.84-17.9 MeV).

A striking observation for the ^{64}Zn target is the consistently low value of the real normalization factor N_R across all energies and for all potentials. For the microscopic DFP-CDM3Y2, N_R varies only between 0.114 and 0.429, indicating a necessary reduction of the bare real potential strength by $57-89\%$. This is even more pronounced than in the ^{58}Ni case and suggests an exceptionally strong repulsive dynamical polarization potential (DPP). The origin of this strong DPP is likely twofold: (1) the persistent coupling to the breakup continuum, and (2) the increased importance of neutron-transfer channels on a target with a higher neutron excess ($N = 34$ for ^{64}Zn vs. $N = 30$ for ^{58}Ni). These channels effectively remove flux from the elastic channel, manifesting as a further reduction in the real potential's attractiveness within the optical model framework.

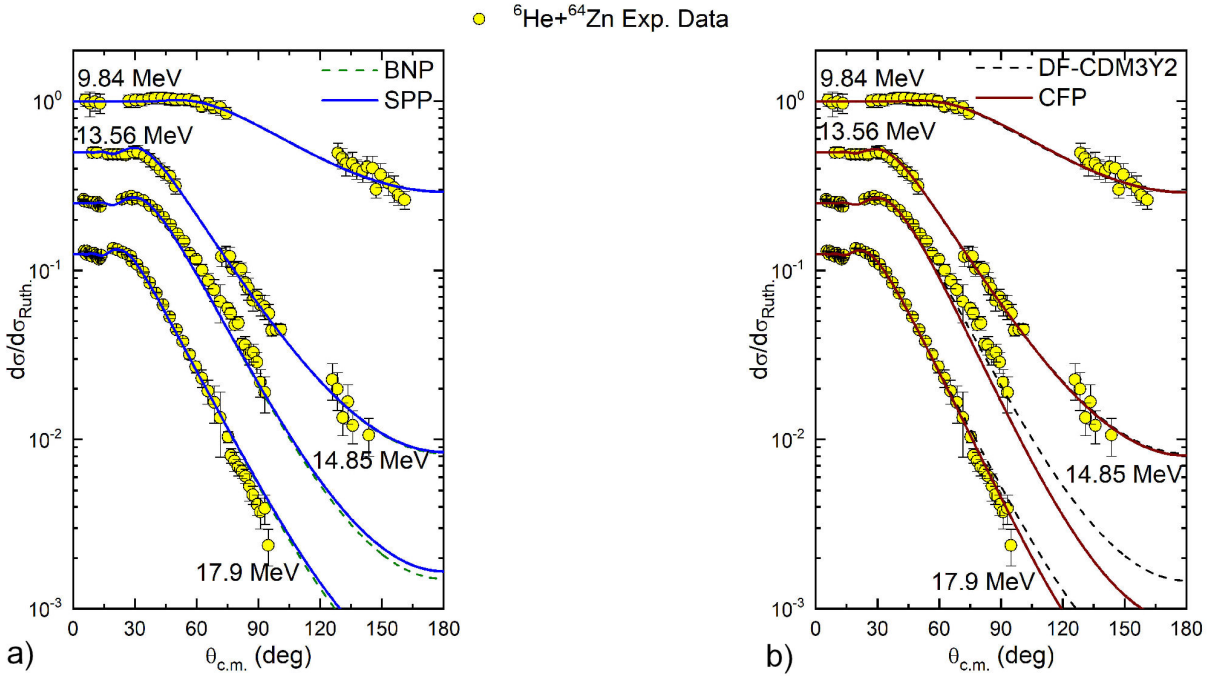

FIGURE 4. Comparison between ^{6}He + ^{64}Zn elastic scattering ADs (circles) and calculations within both BNP and SPP2 presented in panel a), while the results within DF-CDM3Y2 and CFP are presented in panel b).

TABLE II. Optimal potential parameters for ^{6}He+^{64}Zn system within BNP, SPP, DFP-CDM3Y2, and CFP. The σ_R values are displayed. with their estimated uncertainties.

E (MeV)		N_R	N_I	χ^2/N	σ_R (mb)
9.84	BNP	0.376 ± 0.098	0.934 ± 0.366	0.34	469 ± 84
	SPP2	0.394 ± 0.094	0.943 ± 0.366	0.35	469 ± 81
	DFP	0.252 ± 0.023	0.635 ± 0.090	0.35	462 ± 32
	CFP	0.160 ± 0.014	0.746 ± 0.059	0.34	460 ± 24
13.56	BNP	0.634 ± 0.048	1.209 ± 0.212	0.44	1322 ± 52
	SPP2	0.668 ± 0.052	1.183 ± 0.215	0.45	1313 ± 53
	DFP	0.429 ± 0.033	0.826 ± 0.155	0.44	1315 ± 53
	CFP	0.195 ± 0.013	1.247 ± 0.185	0.38	1368 ± 60
14.85	BNP	0.328 ± 0.010	0.376 ± 0.012	19.83	1123 ± 11
	SPP2	0.332 ± 0.001	0.367 ± 0.012	19.33	1118 ± 7
	DFP	0.222 ± 0.006	0.259 ± 0.008	19.92	1123 ± 10
	CFP	0.184 ± 0.005	0.421 ± 0.011	25.01	1151 ± 11
17.9	BNP	0.169 ± 0.005	0.450 ± 0.007	24.20	1386 ± 7
	SPP2	0.180 ± 0.005	0.445 ± 0.006	24.68	1382 ± 6
	DFP	0.114 ± 0.003	0.310 ± 0.004	24.10	1385 ± 5
	CFP	0.073 ± 0.002	0.514 ± 0.006	24.38	1417 ± 6

The behavior of the imaginary part reveals a non-monotonic energy dependence that offers key insights. At the lowest energy (9.84 MeV), a significant imaginary strength is already required ($N_I \sim 0.63 - 0.94$), which is larger than the corresponding value for ^{58}Ni at 9 MeV. This implies that absorption channels, including breakup, become active at a lower relative energy for the ^{64}Zn target. As the energy increases to 13.56 MeV, N_I reaches values around $0.8 - 1.2$, showing an enhancement near the Coulomb barrier–a potential signature of the BTA. However, a striking deviation is observed at 14.85 and 17.9 MeV, where N_I drops markedly to 0.259 and 0.310 (for DFP-CDM3Y2), respectively. This significant decrease in the required absorption strength above the barrier is counter-intuitive if breakup were the sole dominant process. It suggests a possible saturation or change in the dominant reaction mechanism. One plausible explanation

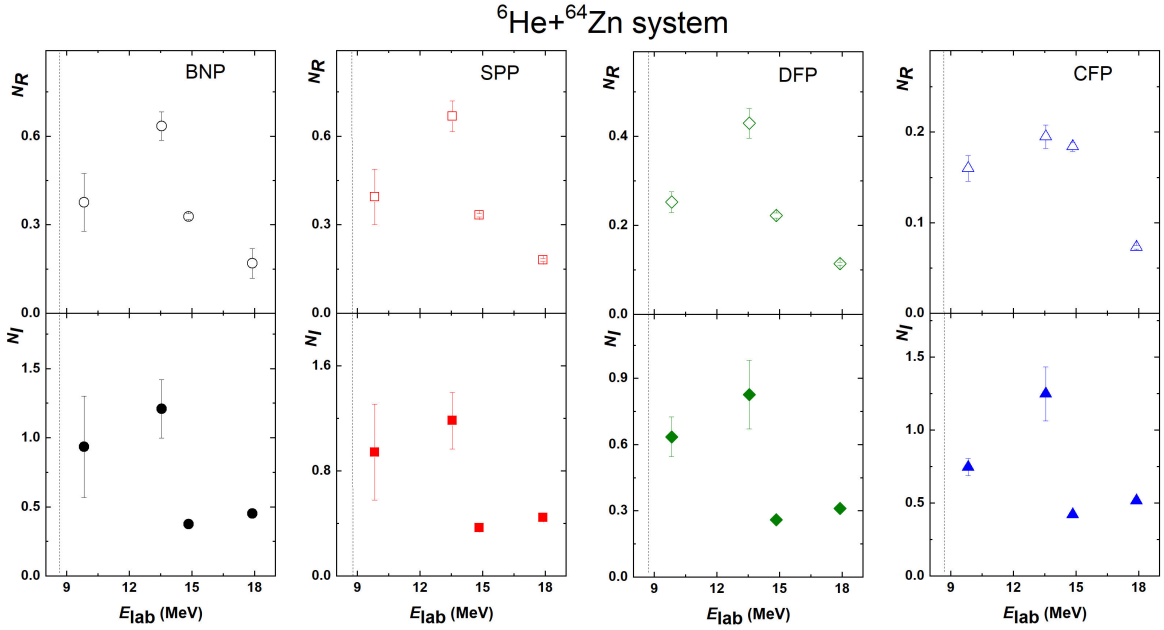

FIGURE 5. Same as Fig. 3, but for the ^{6}He + ^{64}Zn system.

is a shift from direct, peripheral breakup–which strongly absorbs partial waves near the grazing angular momentum– to more penetrative processes like fusion or direct reactions that occur at smaller impact parameters. Alternatively, it may indicate that the simple renormalization of a static, volume-type imaginary potential becomes inadequate at these higher energies, where the absorption becomes more surface-localized or where specific channel couplings interfere destructively in the elastic channel.

The quality of the fits, as indicated by the χ^2/N values, is excellent at 9.84 and 13.56 MeV ($\chi^2/N \sim 0.34 - 0.45$). However, it deteriorates markedly at 14.85 and 17.9 MeV, with χ^2/N values jumping to $\sim 20 - 25$. This significant increase supports the interpretation that the optical model with a renormalized folded potential reaches its limit at these energies. The angular distributions at these energies (see Fig. 4) likely possess finer details that cannot be captured without explicitly including the dynamic coupling to the continuum and other direct channels.

Comparing the models, the CFP again stands out. It consistently produces the largest reaction cross-sections (σ_R) across all energies. For example, at 17.9 MeV, σ_R(CFP) = 1417 mb, compared to 1385 mb for DFP-CDM3Y2. This reinforces the finding from the ^{58}Ni analysis: the explicit α+2n cluster model inherently incorporates more reaction flux, likely by better simulating the peripheral nature of interactions involving the halo neutrons. The fact that this difference persists for ^{64}Zn confirms that cluster degrees of freedom are crucial, regardless of the moderate increase in target charge and mass from ^{58}Ni.

To examine the energy dependence of the optical potential parameters for the ^{6}He + ^{64}Zn system, Fig. 5 presents the N_R and N_I normalization factors as functions of $E_{\rm lab}$, following the same format as Fig. 3. The vertical dashed line at $E_{\rm lab} \sim 8.66$ MeV indicates the laboratory energy corresponding to the Coulomb barrier in the center-of-mass frame ($V_B = 7.92$ MeV).

The upper panel of Fig. 5 shows the real normalization factor N_R. Notably, N_R is consistently low across all energies and potentials, with values typically between 0.07 and 0.67. This strong suppression indicates a pronounced repulsive DPP for this system. The N_R values show some energy dependence: they increase from approximately $0.25-0.40$ at 9.84 MeV to 0.43-0.67 at 13.56 MeV, then decrease again to 0.07-0.18 at 17.9 MeV. This non-monotonic behavior mirrors that observed for the ^{58}Ni target but with generally stronger suppression, possibly reflecting the increased neutron excess of the ^{64}Zn target (N=34) compared to ^{58}Ni ($N = 30$), which may enhance neutron transfer channels and further reduce the real potential strength.

The lower panel of Fig. 5 displays the imaginary normalization factor N_I. At 9.84 MeV, which is above the barrier (8.66 MeV), N_I values are already substantial (0.64-0.94), indicating that breakup channels are active. As energy increases to 13.56 MeV, N_I rises to values of 0.83-1.25, consistent with the BTA. However, at higher energies (14.85 and 17.9 MeV), N_I decreases markedly to $0.26 - 0.51$ for most potentials. This decrease above the barrier is notable and suggests a possible saturation or change in the dominant reaction mechanism. The ^{6}He + ^{64}Zn system thus presents an intermediate case between the lighter ^{58}Ni and heavier ^{120}Sn targets. The BTA signature is present, with enhanced imaginary strength above the barrier, but the decrease in N_I at the highest measured energies suggests a more complex energy dependence than a simple monotonic increase.

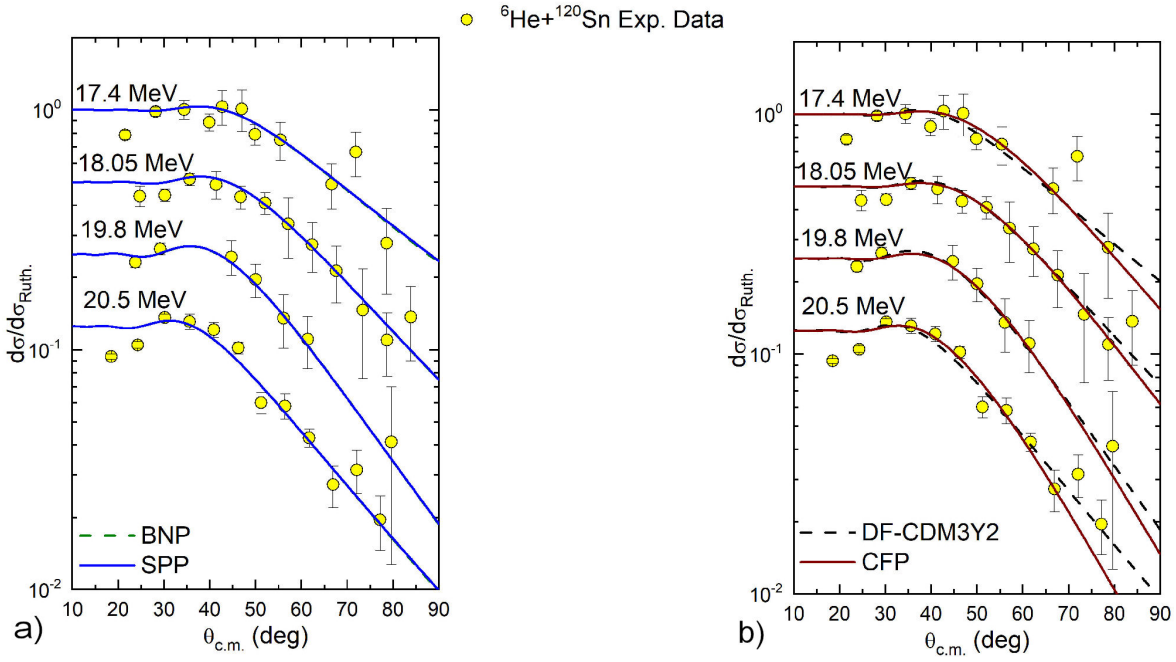

FIGURE 6. Comparison between ^{6}He + ^{120}Sn elastic scattering ADs (circles) and calculations within both BNP and SPP2 presented in panel a), while the results within DF-CDM3Y2 and CFP are presented in panel b).

TABLE III. Optimal potential parameters for ^{6}He+^{120}Sn systems within BNP, SPP2, DFP-CDM3Y2, and CFP. The σ_R values are displayed with their estimated uncertainties.

E (MeV)	Model	N_R	N_I	χ^2/N	σ_R (mb)
17.4	BNP	0.100 ± 0.311	2.000 ± 1.175	4.49	1436 ± 247
	SPP2	0.100 ± 0.327	2.000 ± 0.434	4.50	1422 ± 123
	DFP	0.100 ± 0.172	1.899 ± 1.781	4.56	1510 ± 289
	CFP	0.100 ± 0.001	1.762 ± 0.004	4.54	1476 ± 2
18.05	BNP	0.546 ± 0.212	1.283 ± 0.369	0.76	1427 ± 122
	SPP2	0.568 ± 0.248	1.287 ± 0.336	0.75	1422 ± 116
	DFP	0.371 ± 0.133	0.854 ± 0.271	0.77	1383 ± 115
	CFP	0.140 ± 0.077	1.356 ± 0.001	0.78	1467 ± 23
19.8	BNP	0.449 ± 0.229	0.609 ± 0.216	0.32	1404 ± 145
	SPP2	0.464 ± 0.173	0.601 ± 0.356	0.32	1399 ± 179
	DFP	0.303 ± 0.127	0.415 ± 0.179	0.33	1386 ± 146
	CFP	0.224 ± 0.173	0.624 ± 0.313	0.40	1415 ± 224
20.5	BNP	0.284 ± 0.088	1.127 ± 0.133	22.59	1662 ± 60
	SPP2	0.300 ± 0.135	1.135 ± 0.239	22.59	1657 ± 98
	DFP	0.200 ± 0.054	0.732 ± 0.093	22.81	1615 ± 58
	CFP	0.112 ± 0.152	1.010 ± 0.001	23.13	1648 ± 56

3.3. ^{6}He+^{120}Sn system

The interaction of the halo nucleus ^{6}He with the heavy, high-Z target ^{120}Sn represents the regime where the long-range Coulomb force is most influential, providing the clearest window into breakup-dominated dynamics. The analysis of the elastic scattering ADs across four near-barrier energies ($17.4 - 20.5$ MeV) reveals extreme and systematic effects, as summarized in Table III and Fig. 6. The most striking feature for this system is the profound and persistent suppression of the real potential strength. Across all energies and theoretical potentials (BNP, SPP2, DFP-CDM3Y2, CFP), the optimal real normalization factor N_R is exceptionally low, often pinned at the search lower bound of 0.10. Even when N_R is allowed to vary, it remains below 0.6, implying a reduction of the bare folding potential by 40-90%. This is the most

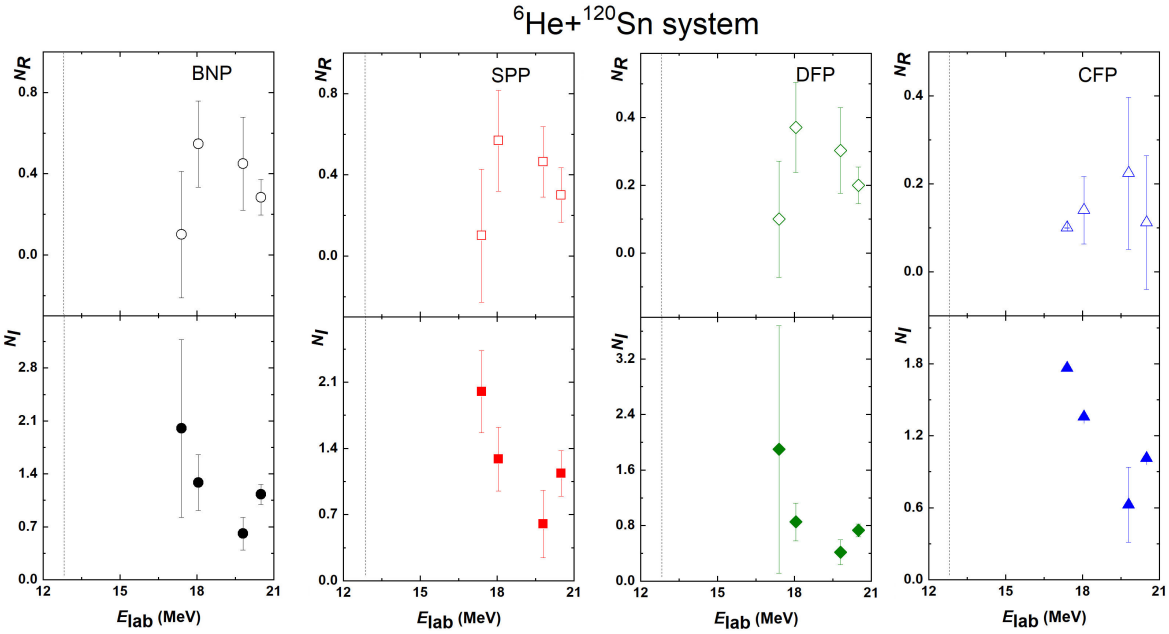

FIGURE 7. Same as Fig. 3, but for the ^{6}He + ^{120}Sn system.

dramatic manifestation of a strong, repulsive DPP observed in this study. For the heavy ^{120}Sn target, the DPP is primarily generated by strong coupling to the Coulomb breakup continuum. The high Coulomb field efficiently excites the fragile ^{6}He projectile into its continuum at large separations, creating a repulsive, long-range polarization that almost completely cancels the attractive real nuclear potential in the peripheral region probed by elastic scattering.

The behavior of the imaginary potential normalization, N_I, is equally revealing and evolves with energy. At the lowest measured energy of 17.4 MeV, which lies well above the Coulomb barrier (12.72 MeV), the fitting process is remarkably insensitive to the value of N_R; an equally good description of the data (χ^2/N ∼4.5) can be achieved with N_R=0.1 or N_R=1.0, provided N_I is large (∼2.0). This indicates that at this energy, the reaction is governed almost entirely by long-range absorption–direct evidence for the BTA. The non-vanishing, and in fact near-maximal, imaginary strength at just above the barrier confirms that breakup channels are open and dominant due to strong Coulomb excitation. As the energy increases to 18.05, 19.8, and 20.5 MeV, the description becomes sensitive to both N_R and N_I. The required N_I values remain high but show a more complex energy dependence, decreasing from ∼1.9 at 17.4 MeV to a minimum around 0.4-0.7 at 19.8 MeV within the DFP model, before increasing again at 20.5 MeV. This non-monotonic trend suggests a transition: at the very lowest energy, pure Coulomb breakup dominates (maximizing peripheral absorption); as the energy rises, nuclear interactions become more significant, potentially altering the breakup mechanism or introducing competing processes like neutron transfer, which may have a different spatial localization of absorption.

The quality of the fits, as measured by χ^2/N, varies significantly with energy. While reasonable descriptions are obtained at 18.05 and 19.8 MeV (χ^2/N ∼0.3-0.8), the fit quality deteriorates at the extremes: at 17.4 MeV (χ^2/N ∼4.5) and especially at 20.5 MeV (χ^2/N ∼23). The poor fit at 20.5 MeV, similar to the issue seen with ^{64}Zn at its highest energy, signals the breakdown of the simple renormalized folding model when the interaction becomes more penetrating and multi-channel effects (beyond a simple, absorptive imaginary potential) become critical.

Among the potentials, the CFP continues its trend of predicting the largest reaction cross-sections (σ_R), particularly at the higher energies. This reinforces the conclusion that an explicit treatment of the α+2n cluster structure is essential to capture the full extent of the reaction flux loss for a halo projectile, even-and perhaps especially-when the interaction is driven by a strong Coulomb field.

For the heavy ^{120}Sn target, the energy dependence of the optical potential parameters reveals the most striking manifestation of the BTA. Figure 7 presents the N_R and N_I normalization factors as functions of $E_{\rm lab}$ for the ^{6}He + ^{120}Sn system. The vertical dashed line at $E_{\rm lab}$ ∼ 12.72 MeV indicates the laboratory energy corresponding to the Coulomb barrier in the center-of-mass frame (V_B = 12.11 MeV).

The upper panel of Fig. 7 shows the real normalization factor N_R. The suppression of N_R is profound, with values typically below 0.6 across all energies and often pinned at or near the lower search bound of 0.1. This extreme suppression reflects a very strong repulsive DPP generated primarily by Coulomb breakup. The high Coulomb field of the ^{120}Sn target efficiently excites the fragile ^{6}He projectile into its continuum at large separations, creating a repulsive, long-range

polarization that almost completely cancels the attractive real nuclear potential in the peripheral region probed by elastic scattering. This effect is strongest for the heaviest target, consistent with the expectation that Coulomb breakup scales with the target charge.

The lower panel of Fig. 7 displays the imaginary normalization factor N_I, which provides the clearest evidence of the BTA in this study. At the lowest measured energy of 17.4 MeV, which is well above the barrier (12.72 MeV), N_I is already large, with values near 1.8-2.0 for most potentials. This indicates that breakup channels are open and dominant. As energy increases to 18.05 MeV, N_I remains elevated but shows some variation depending on the potential. At 19.8 MeV, N_I decreases to values around 0.4-0.6 for BNP, SPP2, and DFP, before rising again at 20.5 MeV. This non-monotonic behavior may reflect a transition in the dominant breakup mechanism or the influence of competing reaction channels as the energy increases. The combination of strong repulsive DPP (small N_R) and large absorption (large N_I) for the ^{120}Sn target represents the most extreme case of breakup-induced polarization among the three targets studied. This reflects the dominant role of the Coulomb field in driving the reaction dynamics of halo nuclei with heavy targets.

3.4. Reaction cross sections for ^{6}He+(^{58}Ni, ^{64}Zn and ^{120}Sn) systems

The reaction cross section (σ_R) extracted from the different potentials is presented in Fig. 8 as function of the reduced energy ($E_{Red} = E_{c.m.}$-V_B), where $E_{c.m.}$ represents the center of mass energy and V_B is the Coulomb barrier height. This representation removes the target-dependent Coulomb barrier shift, allowing for a direct comparison of the reaction dynamics across the three targets. The σ_R values exhibit a systematic increase with increasing reduced energy for all targets, as detailed in Tables I- III and illustrated in Fig. 8. This trend is physically expected, as higher reduced energies enhance the

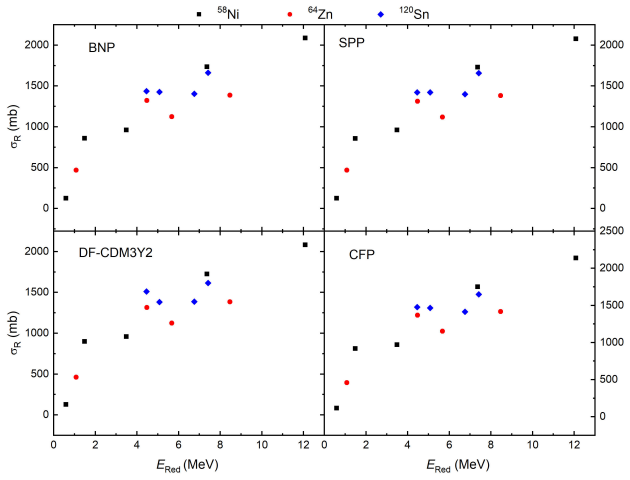

FIGURE 8. Extracted reaction cross section values for ^{6}He scattered from ^{58}Ni, ^{64}Zn, and ^{120}Sn targets within BNP, SPP2, DF-CDM3Y2, and CFP as functions of the reduced energy.

probability of both non-elastic processes (breakup, transfer, and fusion) and enable deeper penetration into the nuclear interior. Notably, the CFP consistently yields the largest σ_R values across all systems and energies, often by a margin of several tens of mb. This systematic offset highlights how the explicit inclusion of the α + 2n cluster configuration in the CFP captures additional reaction flux–likely from peripheral breakup and transfer channels–that is not fully accounted for by the structureless density-folding models. The energy dependence of σ_R further supports the presence of the BTA: the particularly rapid rise of σ_R just above the Coulomb barrier coincides with the strong enhancement of the imaginary potential observed in the optical model analysis.

3.5. Parameter uncertainties and statistical compatibility

We note that in some cases, particularly at lower energies or for specific potentials, the fitting uncertainties reported in Tables I- III for the normalization parameters (N_R and N_I) can be comparable to or even exceed the parameter values themselves. This phenomenon has several origins:

a. Parameter insensitivity at certain energies: At energies just above the Coulomb barrier (*e.g.*, ^{6}He + ^{58}Ni at 9 MeV), the elastic scattering ADs are primarily sensitive to the extreme tail of the nuclear potential. In this region, variations in the potential strength can be partially compensated by adjustments in the other parameter, leading to large correlated uncertainties in the individual N_R and N_I values despite a well-defined minimum in the χ^2 hypersurface.

b. Strong parameter correlation: The real and imaginary normalization factors are not independent; large changes in N_R can often be accommodated by modest adjustments in N_I without significantly affecting the fit quality, particularly when the AD lacks detailed structure (*e.g.*, at the lowest energies or most forward angles). This correlation inflates the individual parameter errors extracted from the covariance matrix.

c. Limited angular range or data points: For some energies, particularly the older data sets, the experimental ADs cover a limited angular range or have fewer data points, which reduces the constraints on the potential parameters.

Importantly, these large uncertainties do not indicate a failure of the fitting procedure. The χ^2/N values in the tables confirm that good descriptions of the data are achieved. Rather, they reflect the physical reality that at certain energies, the elastic scattering observable is not sufficiently sensitive to independently determine both N_R and N_I with high precision.

Following the minimization, the optimal parameters N_R and N_I with their associated uncertainties ΔN_R and ΔN_I were obtained from the covariance matrix produced by

SFRESCO code. To estimate the uncertainty in the reaction cross section (σ_R) arising from the uncertainties in the normalization parameters, we adopted a practical approach. For each potential, energy, and target system, we performed an additional optical model calculation using the shifted parameters $N_R + \Delta N_R$ and $N_I + \Delta N_I$. The absolute difference between the σ_R obtained from this shifted parameter set and the σ_R obtained from the optimal parameters was taken as the estimated uncertainty $\Delta\sigma_R$. This method provides a one-sided estimate of the sensitivity of σ_R to the parameter uncertainties. A full error propagation accounting for parameter correlations would require access to the full covariance matrix and is beyond the scope of the present work. Nevertheless, this approach offers a reasonable indication of the scale of the uncertainty and is consistent with methods sometimes used in optical model analyses when full covariance information is not available. The resulting $\Delta\sigma_R$ values are presented alongside the central σ_R values in Tables I- III.

To check whether the differences in σ_R values among the four potentials are statistically meaningful, we first examine the estimated uncertainties ($\Delta\sigma_R$) presented in Tables I- III. These uncertainties reflect the sensitivity of σ_R values to the uncertainties in the normalization parameters N_R and N_I.

For cases where the parameter uncertainties are small (*e.g.*, ^{6}He + ^{64}Zn at 14.85 and 17.9 MeV, and ^{6}He + ^{120}Sn at 20.5 MeV for BNP and DFP), the estimated $\Delta\sigma_R$ values are correspondingly small, typically 1-2 % of the central σ_R value. For cases where the parameter uncertainties are large (*e.g.*, ^{6}He + ^{58}Ni at 9 MeV for SPP2 and DFP, or ^{6}He + ^{120}Sn at 17.4 MeV for DFP), the estimated $\Delta\sigma_R$ values become substantial, reflecting the poor constraint on the potential parameters at these energies. Using these estimated uncertainties, we examine the statistical compatibility of the cross sections from different potentials. The analysis reveals the following:

- For the ^{6}He + ^{58}Ni system, all fifteen comparisons show statistical compatibility. The differences between CFP and the other potentials are smaller than the combined uncertainties at every energy.
- For the ^{6}He + ^{64}Zn system, the results are mixed. At 9.84 MeV, all three comparisons are statistically compatible. At 13.56 MeV, the differences are comparable to the combined uncertainties, suggesting marginal significance. At 14.85 and 17.9 MeV, where the estimated uncertainties are very small, the differences exceed the combined uncertainties, indicating statistically significant differences at these specific energies.
- For the ^{6}He + ^{120}Sn system, all twelve comparisons show statistical compatibility. The differences between CFP and the other potentials are smaller than the combined uncertainties at all energies.

The statistically significant differences are observed only for the ^{6}He + ^{64}Zn system at 14.85 and 17.9 MeV (six comparisons), with marginal significance at 13.56 MeV (three comparisons). For the ^{58}Ni and ^{120}Sn systems, all differences are statistically compatible.

Given this mixed picture at the individual energy level, we base our conclusion primarily on the systematic consistency of the observed trend across the entire dataset. The CFP yields the largest reaction cross section in all thirty-nine comparisons examined in this study, spanning three target nuclei, all measured energies, and comparisons with each of the other three potentials (BNP, SPP2, and DFP-CDM3Y2). The observation that the CFP yields the largest value in every single case, despite the statistical compatibility at most individual energies, provides meaningful evidence for the role of cluster degrees of freedom in describing the scattering dynamics of this halo nucleus.

4. Summary and conclusions

A comparative analysis of ^{6}He elastic scattering from ^{58}Ni, ^{64}Zn, and ^{120}Sn targets at energies in the vicinity of the Coulomb barrier has been performed using a hierarchy of microscopic and cluster-based optical potentials: the double folding potential (DFP) with the CDM3Y2 interaction, the São Paulo potential (SPP2), the Brazilian nuclear potential (BNP), and a cluster folding potential (CFP) that explicitly incorporates the α+ 2n structure of ^{6}He. By systematically fitting the available ADs and extracting the energy dependence of the optical model parameters, we have identified several key features of the reaction dynamics induced by this two neutron halo nucleus. It is important to note that for all three target systems, the measured energies lie above the Coulomb barrier. Consequently, the present analysis probes the reaction dynamics in the above barrier regime, where nuclear interactions play a significant role alongside Coulomb effects. The principal findings are as follows:

1. Strong Repulsive Dynamical Polarization Potential (DPP): For all targets, a significant reduction in the real potential normalization ($N_R < 1$) is required to describe the data. This effect, most pronounced for the heavy ^{120}Sn target, signals the presence of a repulsive DPP generated by the strong coupling of the elastic channel to the breakup continuum. The DPP effectively renormalizes the bare folding potential, demonstrating how the fragile, extended structure of ^{6}He dynamically modifies the real part of the nucleus-nucleus interaction.

2. Breakup Threshold Anomaly (BTA): Clear signatures of the BTA are observed, particularly for ^{120}Sn, where a large imaginary strength ($N_I \approx 2$) persists even at the lowest measured energy, which lies above the barrier. This indicates that breakup channels - dominantly Coulomb induced for heavy targets - are strongly active even at energies just above the barrier. For the medium

mass targets (^{58}Ni and ^{64}Zn), the imaginary part exhibits a non-monotonic energy dependence, suggesting an evolution of the dominant reaction mechanism as the energy increases.

3. Systematic Behavior of the Cluster Folding Potential (CFP): The CFP, which explicitly treats ^{6}He as an α-core plus two valence neutrons, systematically yields the largest reaction cross sections across all systems and energies, doing so in all thirty-nine comparisons examined in this study. Uncertainty analysis reveals that in thirty of these comparisons, the differences are statistically compatible within the estimated uncertainties. Statistically significant differences are observed only for the ^{6}He + ^{64}Zn system at 14.85 and 17.9 MeV (six comparisons), with marginal significance at 13.56 MeV (three comparisons). For the ^{58}Ni and ^{120}Sn systems, all differences are statistically compatible. Thus, while the CFP exhibits a consistent tendency to produce larger σ_R, the effect is modest and, in many cases, comparable to statistical uncertainties. Nevertheless, the systematic trend-observed without exception-provides meaningful evidence for the role of cluster degrees of freedom in describing the scattering dynamics of this halo nucleus.

4. Limitations of Renormalized Folding Models: The deterioration of fit quality (high χ^2/N) at the highest energies for ^{64}Zn and ^{120}Sn indicates the limitations of simple optical potentials with renormalized folded forms. When the interaction becomes more penetrating and multichannel couplings grow stronger, a static, energy independent imaginary potential is no longer sufficient. This underscores the necessity of more advanced, dynamic frameworks - such as continuum discretized coupled channels (CDCC) calculations - for a complete description of halo nucleus collisions, especially at energies well above the Coulomb barrier.

5. Target Dependence of Reaction Mechanisms: The comparative analysis reveals a clear progression in the role of the Coulomb field. For the lightest target (^{58}Ni), nuclear induced breakup and transfer dominate above the barrier. For the intermediate ^{64}Zn, both Coulomb and nuclear contributions are significant, leading to a complex energy dependence of the imaginary potential. For ^{120}Sn, Coulomb breakup prevails, producing the strongest DPP and the clearest BTA signature, even at energies above the barrier.

In summary, the reaction dynamics of the halo nucleus ^{6}He are acutely sensitive to the Coulomb field of the target, with breakup coupling dictating the energy dependence and magnitude of the effective optical potential in the above barrier regime. This study provides a systematic, multipotential benchmark for understanding elastic scattering of weakly bound, cluster structured projectiles and reinforces the need for structure informed, dynamic reaction models in the description of exotic nuclei. The insights gained here not only illuminate the specific case of ^{6}He but also offer a foundation for future investigations of more complex, neutron rich halo systems.

1. L. R. Gasques *et al.*, Experimental determination of the surface density for the ^{6}He exotic nucleus, *Phys. Rev. C* **67** (2003) 024602, https://doi.org/10.1103/PhysRevC.67.024602
2. R. E. Warner *et al.*, Elastic scattering of 10 MeV ^{6}He from ^{12}C, Ni, and ^{197}Au, *Phys. Rev. C* **51** (1995) 178, https://doi.org/10.1103/PhysRevC.51.178
3. V. Morcelle *et al.*, Four-body effects in the ^{6}He+^{58}Ni scattering, *Phys. Lett. B* **732** (2014) 228,http://dx.doi.org/10.1016/j.physletb.2014.03.043
4. A. Di Pietro *et al.*, Reactions induced by the halo nucleus ^{6}He at energies around the Coulomb barrier, *Phys. Rev. C* **69** (2004) 044613, https://doi.org/10.1103/PhysRevC.69.044613
5. J. P. Fernández-García *et al.*, Breakup mechanisms in the ^{6}He+^{64}Zn reaction at near-barrier energies, *Phys. Rev. C* **99** (2019) 054605, https://doi.org/10.1103/PhysRevC.99.054605.
6. P. N. de Faria *et al.*, Elastic scattering and total reaction cross section of ^{6}He+^{120}Sn, *Phys. Rev. C* **81** (2010) 044605, https://doi.org/10.1103/PhysRevC.81.044605.
7. X.-W. Su *et al.*, Global ^{6}He optical model potential, *Int. J. Mod. Phys. E* **25** (2016) 1650033, https://doi.org/10.1142/S0218301316500336.
8. H. Guo *et al.*, Microscopic optical potential for ^{6}He, *Phys. Rev. C* **95** (2017) 034614, https://doi.org/10.1103/PhysRevC.95.034614.
9. R. Lichtenthäler *et al.*, Elastic scattering of neutron halo projectiles, *Few-Body Syst.* **56** (2015) 767, https://doi.org/10.1007/s00601-015-0987-7.
10. P. Descouvemont, Low-energy ^{6}He scattering in a microscopic model, *Phys. Rev. C* **93** (2016) 034616, https://doi.org/10.1103/PhysRevC.93.034616.
11. I. J. Thompson, Coupled reaction channels calculations in nuclear physics, *Comput. Phys. Rep.* **7** (1988) 167, https://doi.org/10.1016/0167-7977(88)90005-6.
12. D. T. Khoa *et al.*, Nuclear incompressibility and density dependent NN interactions in the folding model for nucleus-nucleus potential, *Phys. Rev. C* **56** (1997) 954, https://doi.org/10.1103/PhysRevC.56.954.
13. L. C. Chamon *et al.*, São Paulo potential version 2 (SPP2) and Brazilian nuclear potential (BNP), *Comput. Phys. Com-*

mun. **267** (2021) 108061, https://doi.org/10.1016/j.cpc.2021.108061.

14. L. C. Chamon *et al*., Nonlocal description of the nucleus-nucleus interaction, *Phys. Rev. Lett.* **79** (1997) 5218, https://doi.org/10.1103/PhysRevLett.79.5218.

15. L. C. Chamon *et al*., Parameter-free account of quasielastic scattering of stable and radioactive nuclei, *Phys. Rev. C* **58** (1998) 576, https://doi.org/10.1103/PhysRevC.58.576.

16. L. C. Chamon, The São Paulo potential, *Nucl. Phys. A* **787** (2007) 198c, https://doi.org/10.1016/j.nuclphysa.2006.12.032.

17. B. V. Carlson and D. Hirata, Dirac-Hartree-Bogoliubov approximation for finite nuclei, *Phys. Rev. C* **62** (2000) 054310, https://doi.org/10.1103/PhysRevC.62.054310.

18. Sh. Hamada and A. A. Ibraheem, Extensive investigation of the ^{6}Li+^{27}Al and ^{6}He+^{27}Al systems using different models, *Phys. Scr.* **97** (2022) 125303, https://doi.org/10.1088/1402-4896/ac9dc9.

19. M. A. G. Alvarez *et al*., A parameter-free optical potential for the heavy-ion elastic scattering process, *Nucl. Phys. A* **723** (2003) 93, https://doi.org/10.1016/S0375-9474(03)01158-8.